NANO LETTERS

Achieving Efficient CO₂ Electrolysis to CO by Local Coordination Manipulation of Nickel Single-Atom Catalysts

Zhaoyang Chen, Chuanhao Wang, Xian Zhong, Hao Lei, Jiawei Li, Yuan Ji, Chunxiao Liu, Mao Ding, Yizhou Dai, Xu Li, Tingting Zheng, Qiu Jiang, Hong-Jie Peng, and Chuan Xia*

ACCESS | Metrics & More | Article Recommendations | Supporting Information

ABSTRACT: Selective electroreduction of CO_2 to C_1 feed gas provides an attractive avenue to store intermittent renewable energy. However, most of the CO_2-to-CO catalysts are designed from the perspective of structural reconstruction, and it is challenging to precisely design a meaningful confining microenvironment for active sites on the support. Herein, we report a local sulfur doping method to precisely tune the electronic structure of an isolated asymmetric nickel−nitrogen−sulfur motif (Ni_1-NSC). Our Ni_1-NSC catalyst presents >99% faradaic efficiency for CO_2-to-CO under a high current density of −320 mA cm^{-2}. In situ attenuated total reflection surface-enhanced infrared absorption spectroscopy and differential electrochemical mass spectrometry indicated that the asymmetric sites show a significantly weaker binding strength of *CO and a lower kinetic overpotential for CO_2-to-CO. Further theoretical analysis revealed that the enhanced CO_2 reduction reaction performance of Ni_1-NSC was mainly due to the effectively decreased intermediate activation energy.

**KEYWORDS:** Electrochemical CO_2 reduction, asymmetric coordination, sulfur, isolated nickel atom
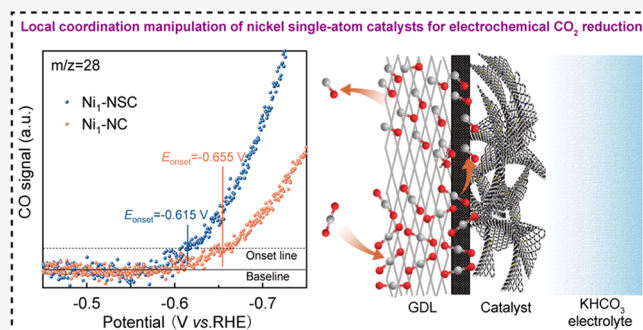
The demanding use of fossil fuels in modern industrial society has produced excessive emissions of CO_2 and caused serious climate-related problems.[1−5] It is highly desirable to develop CO_2 utilization technologies, such as electrochemical CO_2 reduction (ECR). ECR is powered by renewable electricity and has been considered to be a promising CO_2 recycling technology that can efficiently convert CO_2 into value-added compounds.[6−9] Among various products from ECR, carbon monoxide (CO) is one of the most valuable products due to its ease of separation and high economic value per electron, and CO can be used as a fundamental feedstock for the production of many essential chemicals via the Fischer−Tropsch chemistry, or as a reducing agent in industrial metallurgy.[10,11] However, operating current catalysts for CO_2-to-CO at a commercially relevant scale remains challenging. Thus, designing a durable catalyst that has a high CO selectivity at large current densities is of paramount importance. In a general CO_2-to-CO process, the carbon atoms of CO_2 molecules (instead of oxygen atoms) are first adsorbed on the catalyst surface and form the *COOH intermediate via a proton-coupled electron transfer process; then, the adsorbed *COOH is further reduced to *CO and ultimately desorbed from the electrode.[12−14] Therefore, ideal CO_2 reduction reaction (CO_2RR) catalysts for CO evolution should not only have a unique electronic structure showing a decreased barrier for *COOH formation and proper binding

strength with the formed *COOH but also bind weakly enough with the produced *CO on the catalyst surface.

To date, great efforts have been made in the search for active and durable CO-efficient catalysts. Nanostructured Ag and Au are state-of-the-art catalysts for the CO_2-to-CO process, but aside from their high activities, their cost and low faradaic efficiency at high current densities limited their wide industrial applications.[15−18] Recently, earth-abundant transition-metal (TM) catalysts, such as Fe, Co, Ni, and Cu, come out as efficient and cheaper catalysts for CO_2-to-CO, but their activity and selectivity are far from satisfactory.[19−21] To address this problem, downsizing TM into individual atoms and tuning their valence states via well-defined supports have been demonstrated to be effective. Specifically, TM single atoms (TM-SAs) anchored on nitrogen-doped carbon carriers are considered to be one of the most promising nonprecious metal catalysts to convert CO_2 into CO.[22−24] The plane-symmetric M−N₄ structure, where the metal center is coordinatively bonded to four N atoms, was shown to act as the active site of
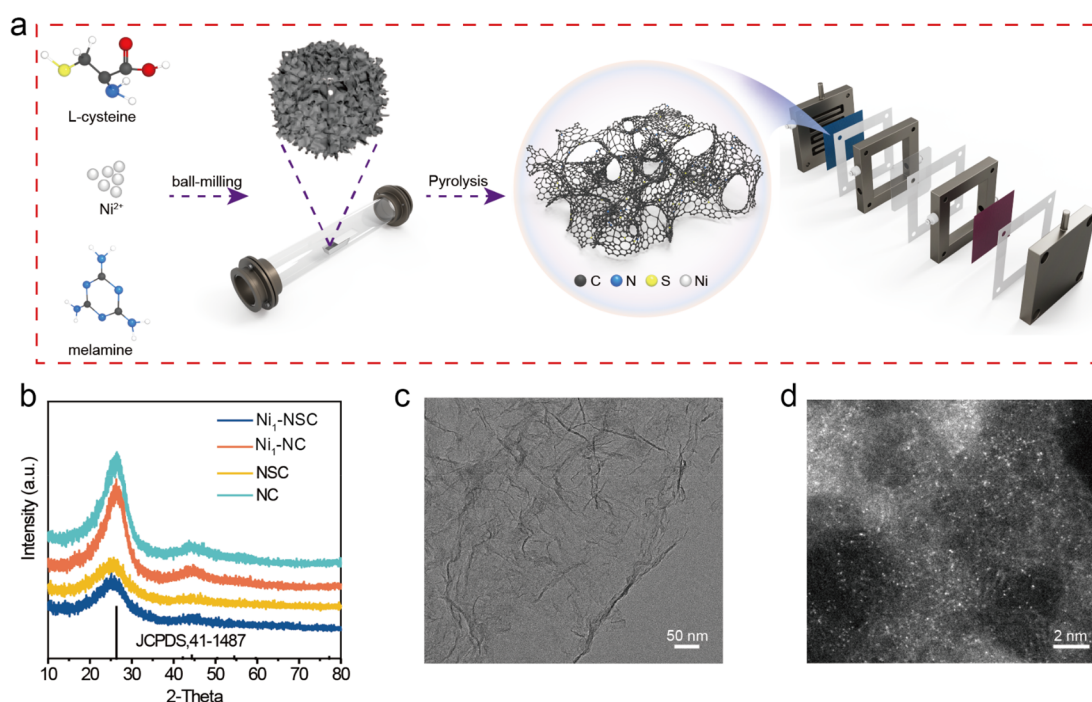
Figure 1. Preparation and structural characterization of Ni₁-NSC. (a) Schematic illustration displaying the preparation process of Ni₁-NSC and application in CO_2RR. (b) X-ray diffraction patterns. (c) TEM image of Ni₁-NSC. (d) HAADF-STEM image of Ni₁-NSC.

CO_2RR and have the advantage to suppress hydrogen evolution reaction (HER).[25,26] However, a symmetrical planar coordinated structure exhibits a large symmetric electron distribution and is not conducive to axial CO_2 adsorption and activation, resulting in high kinetic overpotentials for CO_2-to-CO. To break the symmetry, heteroatoms that have weaker electronegativity toward N can be doped, which can coordinate directly with metal centers and tune the catalytic activity by adjusting the electron-withdrawing/donating properties.[27] The latest research shows that sulfur is a good heteroatom candidate, since sulfur doping is more conducive to promoting the dissociation of water and offers enough protons to convert CO_2 into *COOH.[28] Herein, we employed a ball-milling strategy to create atomically dispersed nickel within a carbon matrix co-doped with nitrogen and sulfur. X-ray absorption spectroscopy (XAS) analysis indicated that the catalyst mainly contained asymmetrically coordinated Ni₁−N₃−S motifs, where the microenvironment of the metal atom was regulated by directly coordinating with the S atom. This novel catalyst shows superior activity and efficiency (nearly 100% CO selectivity at −320 mA cm⁻² in a flow cell) over the traditional Ni₁−N₄ moiety. *In situ* attenuated total reflection surface-enhanced infrared absorption spectroscopy (ATR-SEIRAS) and differential electrochemical mass spectrometry (DEMS) suggest that the asymmetrically coordinated Ni₁−N₃−S sites show a lower kinetic overpotential for CO_2-to-CO and ensure improved CO yield at high current densities. Density functional theory (DFT) calculations further reveal that the enhanced activity and selectivity are attributed to the optimal Gibbs free energy of the *COOH intermediate on the Ni₁−N₃−S sites. Overall, this work demonstrates the significant selectivity and activity advantage of the Ni₁-NSC catalyst and provides unique insights into the design of other asymmetrically coordinated active sites for CO_2RR.

We synthesized the Ni₁-NSC catalyst by grinding a mixture of L-cysteine, melamine, and nickel nitrate into a homogeneous precursor, followed by a two-step high-temperature calcination under an Ar atmosphere (Figure 1a). For comparison, Ni₁-NC was prepared in the same procedure, whereas L-cysteine was replaced by L-alanine. The corresponding catalysts without metals are denoted as NSC and NC. We first investigated the crystallinity and crystalline phase of the catalyst by using X-ray diffraction (XRD), and these four catalysts display similar main diffraction peaks at 26.2° and 43.6°, which were assigned to the (002) and (101) planes of graphitic carbon (Figure 1b). No diffraction peaks for residual Ni, NiN$_x$, or NiC$_x$ were detected in either the Ni₁-NSC or Ni₁-NC samples. On the other hand, Raman spectroscopy shows a higher I_D/I_G ratio of Ni₁-NSC (1.002) compared with Ni₁-NC (0.964), suggesting its more disordered carbon structure (Figure S1). The typical morphology of Ni₁-NSC exhibits thin layered structures, and no particles or clusters were observed (Figure 1c and Figure S2a,b). Energy dispersive spectroscopy (EDS) revealed that C, N, S, and Ni were distributed uniformly across the entire carbon support (Figure S2c,d). The mass ratio of Ni within different samples was measured using inductively coupled plasma optical emission spectroscopy (ICP-OES), showing 0.486 and 0.424 wt % for Ni₁-NSC and Ni₁-NC, respectively. The nanostructure of Ni₁-NSC was further revealed by aberration-corrected high-angle annular dark field scanning transmission electron microscopy (HAADF-STEM), and monodispersed Ni atoms were confirmed by the isolated bright dots across the entire substrate (Figure 1d). Additional morphology and mapping analyses of the four catalysts are shown in Figures S2−S5.

We further performed X-ray photoelectron spectroscopy (XPS) to analyze the chemical states and bonding configurations of the as-synthesized catalysts. The Ni 2p spectrum of the Ni₁-NSC sample shows a positive shift of the Ni 2p$_{3/2}$ main peak (854.9 eV) relative to Ni metal (852.6 eV), indicating the positive oxidation state of single Ni atoms (Figure S6a).[29] The C 1s spectrum displays an asymmetric shape that can be
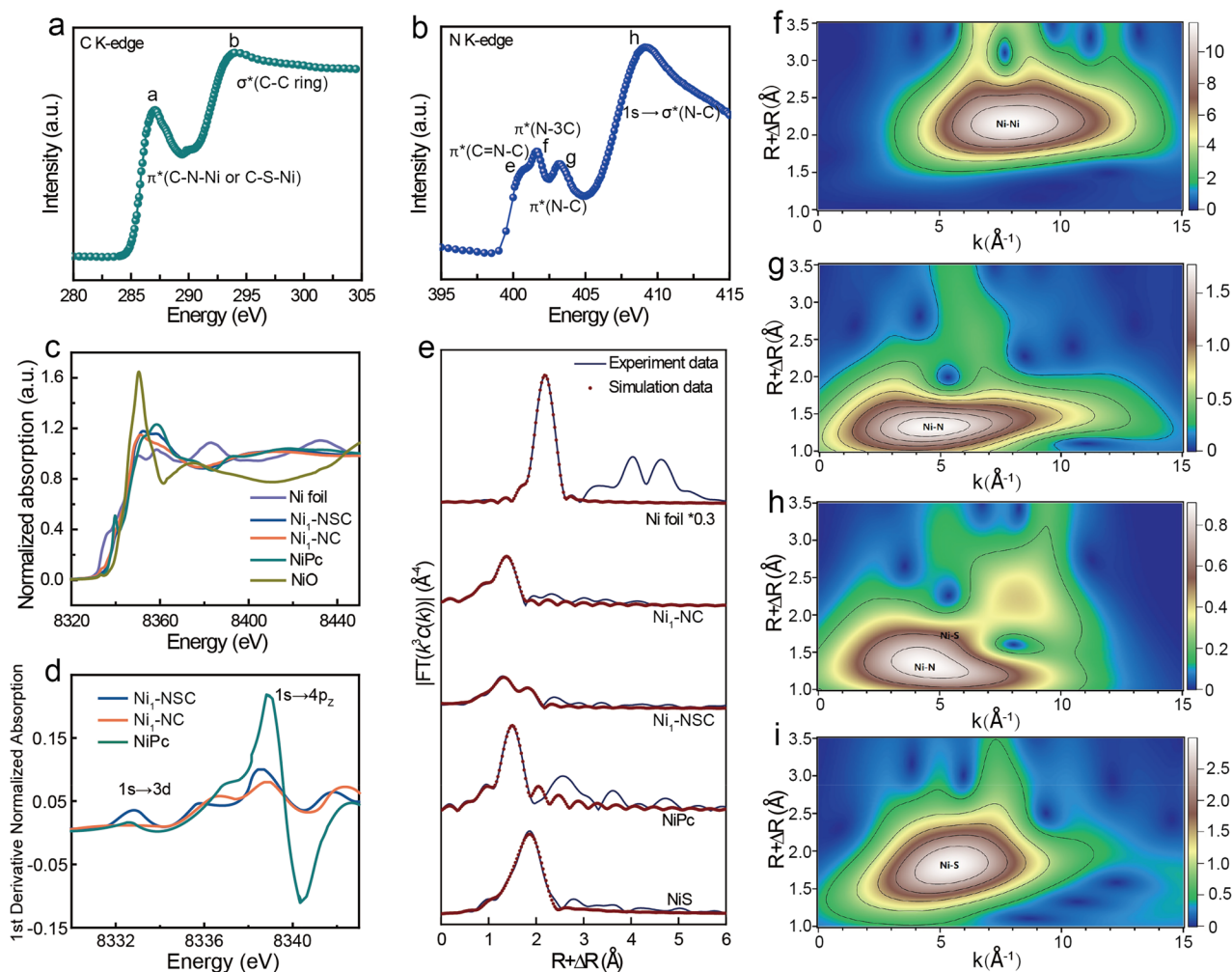
Figure 2. Structural characterization of catalysts. (a) C *K*-edge XANES spectra for Ni_1-NSC and (b) N *K*-edge XANES spectra for Ni_1-NSC. (c) The experimental Ni *K*-edge XANES spectra of Ni_1-NSC, Ni_1-NC, and the references (Ni foil, NiPc, and NiO). (d) First derivative of the pre-edge region of spectra in Ni_1-NSC, Ni_1-NC, and NiPc. (e) Fourier transformed EXAFS spectra in the *R* space and the corresponding FT-EXAFS fitting curves. (f−i) WT-EXAFS plots of Ni foil, Ni_1-NC, Ni_1-NSC, and NiS.

separated into two C species, including C=C (284.6 eV) and C—C/C=N (285.4 eV) (Figure S6b). The high-resolution S 2p XPS spectrum shows two main peaks centered at 163.7 and 164.9 eV, which were assigned to S $2p_{3/2}$ and S $2p_{1/2}$, respectively (Figure S6c).[30] Afterward, soft X-ray absorption near-edge structure (XANES) spectroscopy was carried out for Ni_1-NSC. The C *K*-edge XANES spectrum (Figure 2a) shows excitation resonances at 287.2 and 293.6 eV, which could be assigned to the dipole transition of the C 1s core electron to the π* (C—N—Ni) or π* (C—S—Ni) and σ* (C—C ring) orbitals.[31] Figure 2b shows the N *K*-edge spectrum and the peak at the lower energy side, and the signals are assigned to the 1s → π* transition of heterocyclic rings (π*(C=N—C)), graphitic 3-fold nitrogen atoms (π*(N–3C)), sp³ N—C bridging among tri-*s*-triazine moieties (π*(N—C)), and the 1s → σ*(N—C) transition, respectively.[32,33] The detailed N 1s spectra in Ni_1-NSC (Figure S6d) can be separated into four N species, including graphitic N (401.3 eV), pyrrolic N (400.6 eV), Ni—N (399.2 eV), and pyridinic N (398.1 eV).[34] Similar results were also obtained for the Ni_1-NC catalyst (Figure S7). Furthermore, X-ray absorption fine structure (XAFS) measurements were carried out to probe the chemical identity of the Ni atoms. In Figure 2c, the absorption edges of Ni_1-NSC and Ni_1-

NC are located between Ni foil and NiO, indicating that the Ni atoms possess positive charges and that the average oxidation state is between the two references. The electronic structures of the catalysts were further studied via the first derivative XANES spectra (Figure 2d). The 1s → 3d transition peaks at 8334 eV are evident on Ni_1-NSC, and the peak intensity is significantly stronger in Ni_1-NSC compared to nickel phthalocyanine (NiPc) or Ni_1-NC. The increased peak intensity in Ni_1-NSC indicates that the Ni microenvironment is not uniformly centrosymmetric and is deviating from the perfect plane-symmetric morphology.[35,36] The Fourier transform (FT) EXAFS spectra of both Ni_1-NSC and Ni_1-NC displayed the main peak at 1.4 Å, which was attributed to the scattering of the Ni—N coordination shell. Notably, no related peak corresponding to the Ni—Ni bond (2.2 Å) was observed in either Ni_1-NSC or Ni_1-NC (Figure 2e and Figure S8). Surprisingly, a shoulder peak located at 1.86 Å was also detected in Ni_1-NSC, and the peak was considered to be derived from the Ni—S scattering. Wavelet transform (WT) plots were further applied to identify the Ni *K*-edge EXAFS for a better visual comparison of the catalysts (Figure 2f−i and Figure S9). It was found that Ni foil displays a prominent Ni—Ni bond at approximately 8.0 Å⁻¹, while Ni_1-NSC and Ni_1-NC
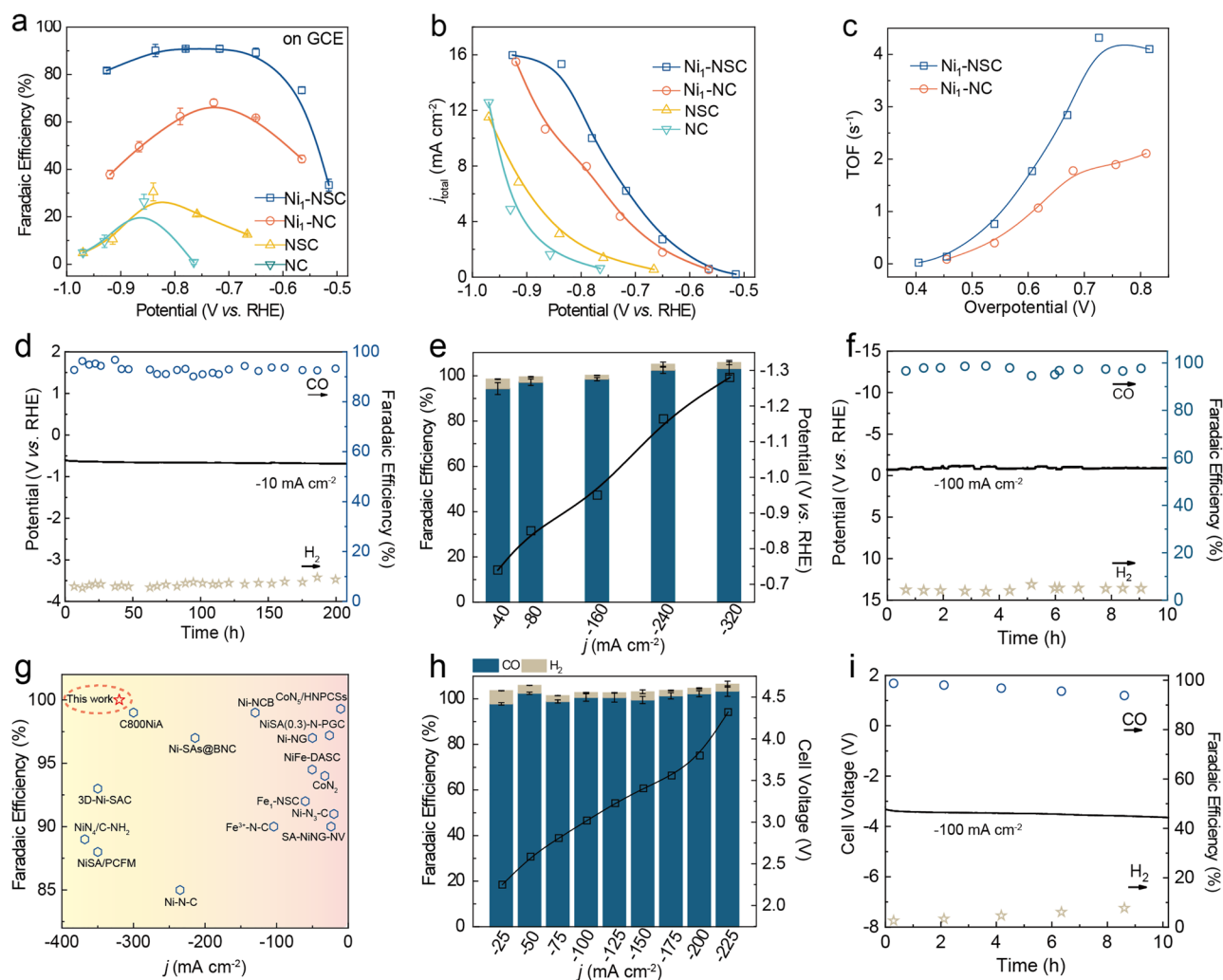
Figure 3. CO_2 electroreduction performance. (a) FEs of CO under different applied potentials for Ni_1-NSC, Ni_1-NC, NSC, and NC. (b) The corresponding $j-V$ curve. (c) TOF of Ni_1-NSC and Ni_1-NC in an H-cell test based on the total mass loaded on the electrode. (d) The CO_2RR stability test of Ni-NSC in an H-cell at -10 mA cm^{-2}. (e) The CO_2 performance of Ni_1-NSC on a gas diffusion layer electrode in a flow cell configuration. (f) Stability test at -100 mA cm^{-2} current density of Ni_1-NSC. (g) Contrasting the FEs and current density values for Ni_1-NSC and other reported single-atom catalysts (Table S2). (h) The corresponding FEs of H_2 and CO in an anion membrane electrode assembly and the corresponding $j-V$ curve without iR-compensation of Ni_1-NSC. (i) Long-term stability test at -100 mA cm^{-2} current density in MEA of Ni_1-NSC.

feature an intensity maximum at 4.5 Å^{-1}, which closely matches the Ni—N bonding. This further indicates that Ni of Ni_1-NSC and Ni_1-NC is atomically dispersed without aggregation. From the WT contour plots of Ni_1-NSC and NiS standards, the WT signals derived from the Ni—S bond are located at ~5.5 Å^{-1}. Quantitative EXAFS fitting curves (Figure 2e and Table S1) indicate that Ni in Ni_1-NSC is coordinated with three N atoms and one S atom with unsymmetrical coordination (Ni_1-N_3-S). For the Ni_1-NC catalyst, four N atom coordination structures were observed.

The CO_2RR performance of the catalysts was first investigated in a three-electrode H-type electrochemical cell using a 0.5 M $KHCO_3$ electrolyte. The catalyst was immobilized on a mirror-polished glassy-carbon electrode (GCE). Online gas chromatography was used to quantify the faradaic efficiency (FE) of gaseous products, and CO was demonstrated to be the major detectable product, while the residual faradaic charge was consumed in the HER process. Notably, the Ni_1-NSC catalyst showed a good CO FE of 73% at a low potential of -0.57 V versus a reversible hydrogen electrode (vs RHE). As the potential becomes more negative,

the selectivity of CO increases, and that of H_2 decreases correspondingly. The FEs of CO were more than 90% over a potential range of -0.65 to -0.82 V vs RHE. Specifically, Ni_1-NSC displays a maximum FE$_{CO}$ of 92% at -0.78 V vs RHE, far surpassing Ni_1-NC (69% at -0.73 V), NSC (32% at -0.84 V), and NC (27% at -0.86 V) (Figure 3a and Figure S10). The results clearly indicated that the Ni_1-N_3-S moieties play a dominating role in the catalytic process. Ni_1-NSC also exhibits a higher overall current density or partial current density of CO (Figure 3b and Figure S11) than that of the studied catalysts. To further evaluate the intrinsic activities of Ni_1-NSC and Ni_1-NC in the CO_2RR, the CO production turnover frequency (TOF) is calculated in accordance with the total mass of the loaded Ni on the electrode (see details in the Experimental Section). As illustrated in Figure 3c, the Ni_1-NSC shows much higher TOF values relative to Ni_1-NC. To examine the stability of Ni_1-NSC, we performed a stationary long-term continuous electrocatalytic test at -10 mA cm^{-2}. After continuous operation for approximately 210 h, the potential and FE$_{CO}$ of the Ni_1-NSC catalyst were almost
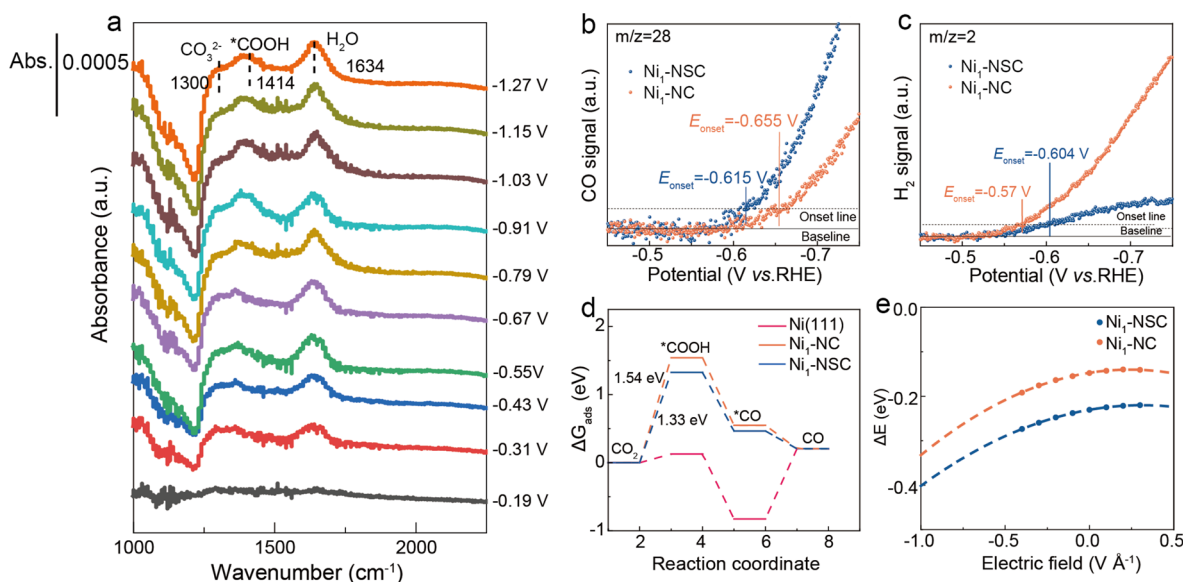
Figure 4. Mechanistic studies of electrochemical CO_2-to-CO conversion. (a) *In situ* ATR-SEIRAS spectra recorded at different applied potentials for Ni_1-NSC, Abs., absorbance. All potentials were calibrated to the RHE scale. (b, c) *In situ* DEMS measurement of CO and H_2 production during the CO_2RR on Ni_1-NSC and Ni_1-NC catalysts. (d) Free-energy diagram for different Ni-centered moieties. (e) The effect of electric field on *CO desorption during electrocatalytic CO_2 reduction of Ni_1-NSC and Ni_1-NC catalysts.

unchanged, suggesting that it possesses excellent intrinsic stability (Figure 3d).

In H-type cells, due to the solubility limit of CO_2, the concomitant HER side reactions are unavoidable. Moreover, the large interelectrode distance and small electrode surface area cannot meet the industrial requirements, making it hard to achieve industrial current densities.[37] To assess the performance of the catalysts for industrial ECR, a flow cell equipped with a gas diffusion electrode (GDE) was applied, where the porous nature of the GDE provides enough three-phase interfaces between the gaseous CO_2 and catalysts.[38] As shown in Figure 3e, Ni_1-NSC achieved a high current density of −320 mA cm^{-2} at −1.28 V vs RHE, and nearly 100% CO selectivity can still be maintained at such high current densities. More importantly, the voltage and FE_{CO} remained unchanged after continuous electrolysis for 10 h at −100 mA cm^{-2} (Figure 3f). We further compared the CO_2RR activity of Ni_1-NSC with other reported transition metal single-atom catalysts and found that Ni_1-NSC exhibited superior activities (Figure 3g, Figure S12a−c, and Table S2). An anion membrane electrode assembly (MEA) device was also used to evaluate the activity of the catalysts. As shown in Figure 3h, significant CO_2RR occurs above the 2.25 V cell voltage and quickly reaches a high current density of −225 mA cm^{-2} at 4.32 V without *iR*-compensation. It was worth noting that the competitive HER reaction is greatly suppressed (2% H_2) due to the fast CO_2 diffusion, and a high CO selectivity (∼99%) was achieved over a wide range of potentials toward other samples (Ni_1-NC, NSC, and NC) (Figure S12d−f). The long-term stability test of Ni_1-NSC manifested that the FE for CO was maintained around 94% after continuous electrolysis at −100 mA cm^{-2} using a MEA device. The slight potential fluctuation was probably due to the membrane degradation or salt precipitation. Additionally, we have also characterized the post-catalysis Ni_1-NSC (Figures S13 and S14). After the stability test, the morphology of the catalyst and its atomic valence state did not change significantly. Collectively, these findings serve as robust evidence affirming its superior stability.

To identify the catalytic mechanism and determine the absorbed surface intermediates with the catalyst, we performed *in situ* ATR-SEIRAS at different potentials (Figure 4a). An obvious broad and asymmetric peak at ∼1414 cm^{-1} was detected, which can be assigned to *COOH.[39] As expected, the *COOH peak gradually appeared and became more apparent as the reduction potential became more negative, proving the direct uptake of CO_2 molecules from the electrolyte and their reduction through the proton-coupled electron transfer process. On the contrary, we did not observe the signal of *CO intermediates on the surface. This could be attributed to the weakened adsorption of *CO intermediates on the Ni_1-NSC surface.[40] *In situ* DEMS was further applied to directly detect the electrochemical formation of CO. As shown in Figure 4b,c, we can clearly see that the introduction of sulfur can significantly lower the kinetic overpotentials and promote CO generation while suppressing the production of H_2. This result is consistent with the results of the CO_2RR test. To elucidate the reaction mechanism of the enhanced CO_2RR activity of Ni_1-NSC, the detailed reaction free-energy diagrams of Ni_1-NSC, Ni_1-NC, and Ni(111) are presented in Figure 4d. Two proton−electron transfer steps are included in electrochemical CO_2-to-CO conversion. Finally, the formed *CO is desorbed from the catalyst surface. Figure S15 shows the possible CO_2RR process of the Ni_1-NSC catalyst. The first protonation step of CO_2 to form *COOH is usually considered to be the rate-determining step. The free-energy change (ΔG) for CO_2-to-*COOH on Ni_1-NSC (1.33 eV) is significantly smaller than that on Ni_1-NC (1.54 eV), proving that the asymmetric coordination structure is conducive to lower the reaction energy barrier. Simultaneously, the free-energy diagrams on Ni nanoparticles (111) for the CO_2RR to CO are also calculated. Although its energy to form *COOH is lower, the desorption energy of *CO is too strong (1.17 eV). Furthermore, we incorporated additional details regarding the impact of the electric field on *CO desorption during the electrocatalytic CO_2 reduction process over Ni_1-NSC and Ni_1-NC catalysts (Figure 4e). From the calculation results, it can

be seen that the intrinsic dipole moment and polarizability of the adsorbents on the two catalysts (Ni_1-NSC and Ni_1-NC) are similar. Therefore, the localized sulfur ligand does not significantly influence the adsorbent's susceptibility to the electric field during the CO_2RR. It means that the electric field has little effect on *CO desorption.

In summary, we have developed a facile way to produce atomically dispersed Ni on N, S co-doped carbon carriers. The catalyst outperformed other Ni-based single-atom catalysts with >99% CO faradaic efficiency and CO partial current densities of > -320 mA cm^{-2}, and an MEA device presents >99% FE_{CO} in a high current density of -225 mA cm^{-2}, underlining a promising future for industrial applications. The critical role of the asymmetric Ni_1-N_3-S sites was demonstrated by the dramatically decreased activity for the Ni_1-N_4 moiety. In situ ATR-SEIRAS and DEMS measurements indicated that the introduction of sulfur can significantly lower the kinetic overpotential and promote faster CO desorption. Further theoretical analysis revealed that the enhanced CO_2RR performance of Ni_1-NSC was mainly due to the effectively decreased intermediate activation energy. This work not only offers new insights into the role of coordination environment regulation in governing the CO_2RR but also provides a reliable design rule for single-atom catalysts.

■ ASSOCIATED CONTENT

ⓢ Supporting Information

The Supporting Information is available free of charge at https://pubs.acs.org/doi/10.1021/acs.nanolett.3c01808.

Figures S1–S15 describing the details of the experimental and theoretical sections, Raman spectra, TEM, STEM images, EDS mappings, HAADF-STEM images, XPS, XANES, electrochemical data, and the reaction mechanism and Tables S1 and S2 describing the EXAFS fitting parameters and a comparison of the CO_2RR performance (PDF)

■ AUTHOR INFORMATION

Corresponding Author

Chuan Xia − School of Materials and Energy, University of Electronic Science and Technology of China, Chengdu 611731, P. R. China; Yangtze Delta Region Institute (Huzhou), University of Electronic Science and Technology of China, Huzhou, Zhejiang 313001, P. R. China; orcid.org/0000-0003-4526-159X; Email: chuan.xia@uestc.edu.cn

Authors

Zhaoyang Chen − School of Materials and Energy, University of Electronic Science and Technology of China, Chengdu 611731, P. R. China; orcid.org/0000-0002-1547-698X

Chuanhao Wang − School of Materials and Energy, University of Electronic Science and Technology of China, Chengdu 611731, P. R. China; orcid.org/0000-0003-0134-5935

Xian Zhong − School of Materials and Energy and Institute of Fundamental and Frontier Sciences, University of Electronic Science and Technology of China, Chengdu 611731, P. R. China

Hao Lei − School of Chemistry and Chemical Engineering, Yancheng Institute of Technology, Yancheng, Jiangsu 224051, P. R. China

Jiawei Li − School of Materials and Energy, University of Electronic Science and Technology of China, Chengdu 611731, P. R. China; orcid.org/0000-0002-9069-7002

Yuan Ji − School of Materials and Energy, University of Electronic Science and Technology of China, Chengdu 611731, P. R. China

Chunxiao Liu − School of Materials and Energy, University of Electronic Science and Technology of China, Chengdu 611731, P. R. China

Mao Ding − School of Materials and Energy, University of Electronic Science and Technology of China, Chengdu 611731, P. R. China

Yizhou Dai − School of Materials and Energy, University of Electronic Science and Technology of China, Chengdu 611731, P. R. China

Xu Li − School of Materials and Energy, University of Electronic Science and Technology of China, Chengdu 611731, P. R. China

Tingting Zheng − School of Materials and Energy, University of Electronic Science and Technology of China, Chengdu 611731, P. R. China

Qiu Jiang − School of Materials and Energy, University of Electronic Science and Technology of China, Chengdu 611731, P. R. China; Yangtze Delta Region Institute (Huzhou), University of Electronic Science and Technology of China, Huzhou, Zhejiang 313001, P. R. China

Hong-Jie Peng − Institute of Fundamental and Frontier Sciences, University of Electronic Science and Technology of China, Chengdu 611731, P. R. China; Yangtze Delta Region Institute (Huzhou), University of Electronic Science and Technology of China, Huzhou, Zhejiang 313001, P. R. China; orcid.org/0000-0002-4183-703X

Complete contact information is available at:
https://pubs.acs.org/10.1021/acs.nanolett.3c01808

Notes

The authors declare no competing financial interest.

■ REFERENCES

(1) Wang, L.; Chen, W.; Zhang, D.; Du, Y.; Amal, R.; Qiao, S.; Wu, J.; Yin, Z. Surface strategies for catalytic CO_2 reduction: from two-dimensional materials to nanoclusters to single atoms. Chem. Soc. Rev. 2019, 48 (21), 5310−5349.

(2) Zheng, T.; Liu, C.; Guo, C.; Zhang, M.; Li, X.; Jiang, Q.; Xue, W.; Li, H.; Li, A.; Pao, C. W.; Xiao, J.; Xia, C.; Zeng, J. Copper-catalysed exclusive CO_2 to pure formic acid conversion via single-atom alloying. Nat. Nanotechnol. 2021, 16 (12), 1386−1393.

(3) Gao, S.; Lin, Y.; Jiao, X.; Sun, Y.; Luo, Q.; Zhang, W.; Li, D.; Yang, J.; Xie, Y. Partially oxidized atomic cobalt layers for carbon

dioxide electroreduction to liquid fuel. *Nature* **2016**, *529* (7584), 68–71.

(4) Huang, J. R.; Qiu, X. F.; Zhao, Z. H.; Zhu, H. L.; Liu, Y. C.; Shi, W.; Liao, P. Q.; Chen, X. M. Single-Product Faradaic Efficiency for Electrocatalytic of CO₂ to CO at Current Density Larger than 1.2 A cm⁻² in Neutral Aqueous Solution by a Single-Atom Nanozyme. *Angew. Chem., Int. Ed.* **2022**, *61* (44), e202210985.

(5) Zhu, Z.; Jiang, T.; Ali, M.; Meng, Y.; Jin, Y.; Cui, Y.; Chen, W. Rechargeable Batteries for Grid Scale Energy Storage. *Chem. Rev.* **2022**, *122* (22), 16610–16751.

(6) Ahmad, T.; Liu, S.; Sajid, M.; Li, K.; Ali, M.; Liu, L.; Chen, W. Electrochemical CO₂ Reduction to C₂₊ Products Using Cu-Based Electrocatalysts: A Review. *Nano Res. Energy* **2022**, *1*, e9120021.

(7) Li, W.; Yin, Z.; Gao, Z.; Wang, G.; Li, Z.; Wei, F.; Wei, X.; Peng, H.; Hu, X.; Xiao, L.; Lu, J.; Zhuang, L. Bifunctional ionomers for efficient co-electrolysis of CO₂ and pure water towards ethylene production at industrial-scale current densities. *Nat. Energy* **2022**, *7* (9), 835–843.

(8) Wu, Y.; Jiang, Z.; Lu, X.; Liang, Y.; Wang, H. Domino electroreduction of CO₂ to methanol on a molecular catalyst. *Nature* **2019**, *575* (7784), 639–642.

(9) Hao, Q.; Zhong, H. X.; Wang, J. Z.; Liu, K. H.; Yan, J. M.; Ren, Z. H.; Zhou, N.; Zhao, X.; Zhang, H.; Liu, D. X.; Liu, X.; Chen, L. W.; Luo, J.; Zhang, X. B. Nickel dual-atom sites for electrochemical carbon dioxide reduction. *Nat. Synth.* **2022**, *1* (9), 719–728.

(10) Zheng, T.; Jiang, K.; Wang, H. Recent Advances in Electrochemical CO₂-to-CO Conversion on Heterogeneous Catalysts. *Adv. Mater.* **2018**, *30* (48), 1802066.

(11) Wang, C.; Fang, W.; Liu, Z.; Wang, L.; Liao, Z.; Yang, Y.; Li, H.; Liu, L.; Zhou, H.; Qin, X.; Xu, S.; Chu, X.; Wang, Y.; Zheng, A.; Xiao, F. S. Fischer–Tropsch synthesis to olefins boosted by MFI zeolite nanosheets. *Nat. Nanotechnol.* **2022**, *17* (7), 714–720.

(12) Pan, Y.; Lin, R.; Chen, Y.; Liu, S.; Zhu, W.; Cao, X.; Chen, W.; Wu, K.; Cheong, W. C.; Wang, Y.; Zheng, L.; Luo, J.; Lin, Y.; Liu, Y.; Liu, C.; Li, J.; Lu, Q.; Chen, X.; Wang, D.; Peng, Q.; Chen, C.; Li, Y. Design of Single-Atom Co-N₅ Catalytic Site: A Robust Electrocatalyst for CO₂ Reduction with Nearly 100% CO Selectivity and Remarkable Stability. *J. Am. Chem. Soc.* **2018**, *140* (12), 4218–4221.

(13) Jiang, K.; Siahrostami, S.; Akey, A. J.; Li, Y.; Lu, Z.; Lattimer, J.; Hu, Y.; Stokes, C.; Gangishetty, M.; Chen, G.; Zhou, Y.; Hill, W.; Cai, W.-B.; Bell, D.; Chan, K.; Nørskov, J. K.; Cui, Y.; Wang, H. Transition-metal single atoms in a graphene shell as active centers for highly efficient artificial photosynthesis. *Chem.* **2017**, *3* (6), 950–960.

(14) Bligaard, T.; Nørskov, J. K.; Dahl, S.; Matthiesen, J.; Christensen, C. H.; Sehested, J. The Brønsted-Evans-Polanyi relation and the volcano curve in heterogeneous catalysis. *J. Catal.* **2004**, *224* (1), 206–217.

(15) Lu, Q.; Rosen, J.; Zhou, Y.; Hutchings, G. S.; Kimmel, Y. C.; Chen, J. G.; Jiao, F. A selective and efficient electrocatalyst for carbon dioxide reduction. *Nat. Commun.* **2014**, *5* (1), 3242.

(16) Zhu, W.; Michalsky, R.; Metin, O.; Lv, H.; Guo, S.; Wright, C. J.; Sun, X.; Peterson, A. A.; Sun, S. Monodisperse Au Nanoparticles for Selective Electrocatalytic Reduction of CO₂ to CO. *J. Am. Chem. Soc.* **2013**, *135* (45), 16833–16836.

(17) Ma, M.; Trzesniewski, B. J.; Xie, J.; Smith, W. A. Selective and Efficient Reduction of Carbon Dioxide to Carbon Monoxide on Oxide-Derived Nanostructured Silver Electrocatalysts. *Angew. Chem., Int. Ed.* **2016**, *128* (33), 9900–9904.

(18) Yoon, Y.; Hall, A. S.; Surendranath, Y. Tuning of silver catalyst mesostructure promotes selective carbon dioxide conversion into fuels. *Angew. Chem., Int. Ed.* **2016**, *55* (49), 15282–15286.

(19) Miao, Z.; Meng, J.; Liang, M.; Li, Z.; Zhao, Y.; Wang, F.; Xu, L.; Mu, J.; Zhuo, S.; Zhou, J. In-situ, C. V. D. synthesis of Ni@N-CNTs/carbon paper electrode for electro-reduction of CO₂. *Carbon* **2021**, *172*, 324–333.

(20) Hori, Y.; Wakebe, H.; Tsukamoto, T.; Koga, O. Electrocatalytic process of CO selectivity in electrochemical reduction of CO₂ at metal electrodes in aqueous media. *Electrochim. Acta* **1994**, *39* (11–12), 1833–1839.

(21) Liu, C.; Cundari, T. R.; Wilson, A. K. CO₂ Reduction on Transition Metal (Fe, Co, Ni, and Cu) Surfaces: In Comparison with Homogeneous Catalysis. *J. Phys. Chem. C* **2012**, *116* (9), 5681–5688.

(22) Gu, J.; Hsu, C.-S.; Bai, L.; Chen, H. M.; Hu, X. Atomically dispersed Fe³⁺ sites catalyze efficient CO₂ electroreduction to CO. *Science* **2019**, *364* (6445), 1091–1094.

(23) Ju, W.; Bagger, A.; Hao, G.-P.; Varela, A. S.; Sinev, I.; Bon, V.; Roldan Cuenya, B.; Kaskel, S.; Rossmeisl, J.; Strasser, P. Understanding activity and selectivity of metal-nitrogen-doped carbon catalysts for electrochemical reduction of CO₂. *Nat. Commun.* **2017**, *8* (1), 944.

(24) Wu, Z.-Y.; Zhu, P.; Cullen, D. A.; Hu, Y.; Yan, Q.-Q.; Shen, S.-C.; Chen, F.-Y.; Yu, H.; Shakouri, M.; Arregui-Mena, J. D.; Ziabari, A.; Paterson, A. R.; Liang, H.-W.; Wang, H. A general synthesis of single atom catalysts with controllable atomic and mesoporous structures. *Nat. Synth.* **2022**, *1* (8), 658–667.

(25) Xu, C.; Zhi, X.; Vasileff, A.; Wang, D.; Jin, B.; Jiao, Y.; Zheng, Y.; Qiao, S.-Z. Highly Selective Two-Electron Electrocatalytic CO₂ Reduction on Single-Atom Cu Catalysts. *Small Struct.* **2021**, *2* (1), 2000058.

(26) Zhang, Y.; Jiao, L.; Yang, W.; Xie, C.; Jiang, H. L. Rational Fabrication of Low-Coordinate Single-Atom Ni Electrocatalysts by MOFs for Highly Selective CO₂ Reduction. *Angew. Chem., Int. Ed.* **2021**, *60* (14), 7607–7611.

(27) Li, X.; Liu, L.; Ren, X.; Gao, J.; Huang, Y.; Liu, B. Microenvironment modulation of single-atom catalysts and their roles in electrochemical energy conversion. *Sci. Adv.* **2020**, *6* (39), eabb6833.

(28) Chen, S.; Li, X.; Kao, C. W.; Luo, T.; Chen, K.; Fu, J.; Ma, C.; Li, H.; Li, M.; Chan, T. S.; Liu, M. Unveiling the Proton-Feeding Effect in Sulfur-Doped Fe-N-C Single-Atom Catalyst for Enhanced CO₂ Electroreduction. *Angew. Chem., Int. Ed.* **2022**, *61* (32), e202206233.

(29) Zheng, T.; Jiang, K.; Ta, N.; Hu, Y.; Zeng, J.; Liu, J.; Wang, H. Large-scale and highly selective CO₂ electrocatalytic reduction on nickel single-atom catalyst. *Joule* **2019**, *3* (1), 265–278.

(30) Zhang, J.; Zhao, Y.; Chen, C.; Huang, Y. C.; Dong, C. L.; Chen, C. J.; Liu, R. S.; Wang, C.; Yan, K.; Li, Y.; Wang, G. Tuning the coordination environment in single-atom catalysts to achieve highly efficient oxygen reduction reactions. *J. Am. Chem. Soc.* **2019**, *141* (51), 20118–20126.

(31) Shang, H.; Zhou, X.; Dong, J.; Li, A.; Zhao, X.; Liu, Q.; Lin, Y.; Pei, J.; Li, Z.; Jiang, Z.; Zhou, D.; Zheng, L.; Wang, Y.; Zhou, J.; Yang, Z.; Cao, R.; Sarangi, R.; Sun, T.; Yang, X.; Zheng, X.; Yan, W.; Zhuang, Z.; Li, J.; Chen, W.; Wang, D.; Zhang, J.; Li, Y. Engineering Unsymmetrically Coordinated Cu-S₁N₃ Single Atom Sites with Enhanced Oxygen Reduction Activity. *Nat. Commun.* **2020**, *11* (1), 3049.

(32) Meng, N.; Ren, J.; Liu, Y.; Huang, Y.; Petit, T.; Zhang, B. Engineering oxygen-containing and amino groups into two-dimensional atomically-thin porous polymeric carbon nitrogen for enhanced photocatalytic hydrogen production. *Energy Environ. Sci.* **2018**, *11* (3), 566–571.

(33) Che, W.; Cheng, W.; Yao, T.; Tang, F.; Liu, W.; Su, H.; Huang, Y.; Liu, Q.; Liu, J.; Hu, F.; Pan, Z.; Sun, Z.; Wei, S. Fast Photoelectron Transfer in (Cring)-C₃N₄ Plane Heterostructural Nanosheets for Overall Water Splitting. *J. Am. Chem. Soc.* **2017**, *139* (8), 3021–3026.

(34) Yang, H. P.; Lin, Q.; Zhang, C.; Yu, X. Y.; Cheng, Z.; Li, G. D.; Hu, Q.; Ren, X. Z.; Zhang, Q. L.; Liu, J. H.; He, C. X. Carbon Dioxide Electroreduction on Single-Atom Nickel Decorated Carbon Membranes with Industry Compatible Current Densities. *Nat. Commun.* **2020**, *11* (1), 593.

(35) Colpas, G. J.; Maroney, M. J.; Bagyinka, C.; Kumar, M.; Willis, W. S.; Suib, S. L.; Mascharak, P. K.; Baidya, N. X-ray spectroscopic studies of nickel complexes, with application to the structure of nickel sites in hydrogenases. *Inorg. Chem.* **1991**, *30* (5), 920–928.

(36) Koshy, D. M.; Chen, S.; Lee, D. U.; Stevens, M. B.; Abdellah, A. M.; Dull, S. M.; Chen, G.; Nordlund, D.; Gallo, A.; Hahn, C.; Higgins, D. C.; Bao, Z.; Jaramillo, T. F. Understanding the Origin of Highly

Selective CO_2 Electroreduction to CO on Ni,N-doped Carbon Catalysts. *Angew. Chem., Int. Ed.* **2020**, *59* (10), 4043−4050.

(37) Perry, M. L.; Newman, J.; Cairns, E. J. Mass transport in gas-diffusion electrodes: a diagnostic tool for fuel-cell cathodes. *J. Electrochem. Soc.* **1998**, *145* (1), 5.

(38) Nguyen, T. N.; Dinh, C. T. Gas diffusion electrode design for electrochemical carbon dioxide reduction. *Chem. Soc. Rev.* **2020**, *49* (21), 7488−7504.

(39) Huang, M.; Deng, B.; Zhao, X.; Zhang, Z.; Li, F.; Li, K.; Cui, Z.; Kong, L.; Lu, J.; Dong, F.; Zhang, L.; Chen, P. Template-Sacrificing Synthesis of Well-Defined Asymmetrically Coordinated Single-Atom Catalysts for Highly Efficient CO_2 Electrocatalytic Reduction. *ACS Nano* **2022**, *16* (2), 2110−2119.

(40) Dunwell, M.; Lu, Q.; Heyes, J. M.; Rosen, J.; Chen, J. G.; Yan, Y.; Jiao, F.; Xu, B. The central role of bicarbonate in the electrochemical reduction of carbon dioxide on gold. *J. Am. Chem. Soc.* **2017**, *139* (10), 3774−3783.